Research Square

Preprints are preliminary reports that have not undergone peer review.
They should not be considered conclusive, used to inform clinical practice,
or referenced by the media as validated information.

Fe-Doped $WO_3/BiVO_4$ Heterojunction as an Efficient Photo-Fenton Catalyst for Tetracycline Degradation: Performance and Mechanism Insight

Junlin Zhu
Lanzhou University of Technology
Meilin Yan
Lanzhou University of Technology
Youcai Zhang
Lanzhou University of Technology
Jinglong Bai
Lanzhou University of Technology
Wangjun Feng
Lanzhou University of Technology
Huining Zhang
Lanzhou University of Technology
Zhiqiang Wei
qianweizuo@163.com
Lanzhou University of Technology

Research Article

Keywords: Fe-doped $WO_3/BiVO_4$, Photo-Fenton reaction , tetracycline, Type-II heterojunction, Wastewater treatment

Posted Date: November 24th, 2026

DOI: https://doi.org/10.21203/rs.3.rs-11561929/v1

License: This work is licensed under a Creative Commons Attribution 4.0 International License.
Read Full License

Additional Declarations: No competing interests reported.

Fe-Doped $WO_3/BiVO_4$ Heterojunction as an Efficient Photo-Fenton Catalyst for Tetracycline Degradation: Performance and Mechanism Insight

Junlin Zhu[a], Zhiqiang Wei[a,b*], Meilin Yan[a],Youcai Zhang[a], Jinglong Bai[a], Wangjun Feng[a]and Huining Zhang[c]

[a] *School of Science, Lanzhou University of Technology, Lanzhou 730050, China*

[b] *State Key Laboratory of Advanced Processing and Recycling of Non-ferrous Metals, Lanzhou University of Technology, Lanzhou 730050, China*

[c] *School of civil and hydraulic engineering, Lanzhou University of Technology, Lanzhou 730050, China*

** Corresponding author.*

E-mail address: qianweizuo@163.com (Z. Wei)

Abstract

Precise modulation of the microstructure and interfacial electronic states of WO_3-based photocatalysts is essential to address the inherent drawbacks of conventional photo-Fenton systems, including rapid charge recombination, narrow pH tolerance and insufficient cycling stability for tetracycline-containing wastewater remediation.

In this work, an Fe-doped WO_3/$BiVO_4$ heterojunction photocatalyst was fabricated via a facile hydrothermal method for efficient visible-light-driven tetracycline (TC) degradation. The tight integration of tetragonal prismatic $BiVO_4$ and flower-like Fe-doped WO_3 constructs intimate heterointerfaces with lattice distortion and enriched oxygen vacancies, which provide abundant active sites and optimize interfacial charge transfer.

The crystal structure, micromorphology and optical properties were systematically characterized by XRD, XPS, TEM and UV-vis DRS. Photo-Fenton tests reveal that the optimal 0.5 $BiVO_4$/Fe-WO_3 (0.5 BFW) sample achieves 94.5% removal of 50 mg/L TC within 60 min under simulated visible light irradiation. Its apparent rate constant is 7.0 times that of pristine WO_3 and 1.35 times that of single Fe-doped WO_3. The catalyst also exhibits wide pH adaptability and excellent reusability after five cycles.

Mechanism analysis indicates that the Type-II band alignment effectively promotes spatial separation of photogenerated carriers and accelerates the Fe^{3+}/Fe^{2+} redox cycle, with superoxide radicals as the dominant reactive species. This work provides a feasible strategy for developing high-performance photo-Fenton catalysts toward alkaline antibiotic wastewater treatment.

Keywords: Fe-doped WO_3/$BiVO_4$; Photo-Fenton reaction ; tetracycline;Type-II heterojunction; Wastewater treatment.

1. Introduction

In recent years, with the rapid development of healthcare, industry and urbanization, global antibiotic consumption has increased dramatically, and antibiotic-induced environmental pollution has become a pressing global environmental issue[1-3]. Antibiotics enter natural water bodies through multiple pathways, including medical wastewater, livestock and poultry farming discharges, aquaculture effluents and municipal sewage. Tetracycline (TC), one of the most widely used broad-spectrum antibiotics, is characterized by high chemical stability, a long half-life and poor biodegradability, enabling its long-term persistence and accumulation in aquatic environments. It not only exerts acute and chronic toxic effects on aquatic organisms, disrupting the community structure and biogeochemical cycles of aquatic ecosystems[4-6], but also accelerates the spread of antibiotic resistance genes via horizontal gene transfer, posing a long-term potential threat to global public health[7,8]. Conventional wastewater treatment processes exhibit limited removal efficiency for low-concentration tetracycline residues. Accordingly, the development of efficient and eco-friendly technologies for the advanced removal of antibiotics is of great practical significance[9].

Compared with traditional treatment technologies, photocatalytic

degradation has emerged as a promising strategy for organic wastewater treatment, owing to its advantages of environmental friendliness, low energy consumption and mild reaction conditions. This technology employs semiconductor materials as photocatalysts; under visible or ultraviolet light irradiation, photogenerated electron–hole pairs are excited and participate in a series of redox reactions, which decompose organic pollutants in water into harmless small molecules such as carbon dioxide and water. Advanced Oxidation Processes (AOPs) can generate highly oxidizing reactive oxygen species (ROS) in situ to rapidly break down the molecular structure of organic contaminants and achieve mineralization, and are currently one of the mainstream technologies for removing trace antibiotic pollutants from water[10].

Among AOPs, the photo-Fenton process combines the dual advantages of photocatalysis and the Fenton reaction. Under light irradiation, the redox cycling of iron species activates hydrogen peroxide to continuously generate strong oxidizing free radicals. This technology features operational simplicity, high energy efficiency and environmental friendliness, and has thus become a research hotspot in the field of antibiotic pollution control[11,12]. Therefore, the development of efficient photo-Fenton catalysts is a key strategy to enhance tetracycline degradation performance.

Tungsten trioxide (WO_3) is an n-type semiconductor with a moderate band gap. Owing to its unique optical, electrical properties and excellent chemical stability, it is regarded as a promising visible-light-driven photocatalyst and has received extensive academic attention. WO_3 exhibits outstanding chemical stability and corrosion resistance in acidic and alkaline aqueous solutions as well as under illumination, and can maintain structural integrity. In addition, it possesses a well-matched band structure and strong hole oxidation capacity, delivering remarkable oxidation and degradation performance toward organic dyes and other pollutants. Nevertheless, pristine WO_3 still has intrinsic drawbacks: constrained by its relatively positive conduction band potential, photogenerated electrons show weak oxygen reduction ability and tend to recombine rapidly with valence band holes. Meanwhile, its low specific surface area and limited surface active sites result in unsatisfactory pollutant adsorption capacity, which further restricts the photocatalytic degradation efficiency. To address these shortcomings, researchers have developed various modification strategies, including elemental doping[13], morphology regulation, surface engineering and heterostructure construction[14].

In addition, bismuth vanadate ($BiVO_4$) is a narrow-bandgap visible-light photocatalyst with great application potential. Its

appropriate band gap, excellent visible-light absorption capacity and chemical stability have attracted widespread attention. Among the various polymorphs of $BiVO_4$, monoclinic scheelite $BiVO_4$ has the narrowest band gap (approximately 2.4 eV) and the highest visible-light photocatalytic activity, and has shown favorable performance in the photocatalytic degradation of antibiotics in water. However, the catalytic activity of single-phase $BiVO_4$ is still limited, and researchers have coupled it with other semiconductors to further enhance performance[15-17].On this basis, this work proposes to dope Fe into the WO_3 lattice and then couple it with $BiVO_4$ to construct a Fe-doped $WO_3/BiVO_4$ composite catalyst with dual modification of ion doping and heterojunction construction. The composite system is designed to achieve a synergistic effect in the photo-Fenton reaction, improve degradation efficiency, and enhance the stability and pH adaptability of the catalyst.

Herein, a series of Fe-$WO_3/BiVO_4$ photocatalysts were prepared via a hydrothermal method. Using tetracycline (TC) as the target pollutant, the photo-Fenton performance of the samples was evaluated under simulated solar irradiation. The effects of H_2O_2 concentration, initial pH and catalyst dosage on the photo-Fenton activity were systematically investigated, and the reaction conditions were optimized

using response surface methodology. The results demonstrate that the construction of the composite can significantly improve the photo-Fenton performance. Combined with radical scavenging experiments, a plausible reaction mechanism for tetracycline degradation over the catalyst was proposed.

2. Experimental Design and Material Synthesis

2.1 Synthesis of materials

2.1.1 Synthesis of Fe-doped WO_3

As shown in **Fig. 1**,0.33 g of $Na_2WO_4 \cdot 2H_2O$ and 0.071 g of Na_2SO_4 were dissolved in a mixed solution containing 16 mL of deionized water and 4 mL of acetic acid under magnetic stirring for 30 min. Then, a certain amount of $FeCl_3 \cdot 6H_2O$ was added to the solution, and the pH was adjusted to 1. After stirring for another 1 h, the mixture was transferred into a 50 mL Teflon-lined autoclave and heated at 160 °C for 2 h. The resulting precipitate was collected and washed alternately with deionized water and ethanol until the supernatant became neutral. Finally, the sample was dried in a vacuum oven at 60 °C overnight to obtain Fe-doped WO_3 nanospheres. Pristine WO_3 was prepared under the same conditions without the addition of Fe source.

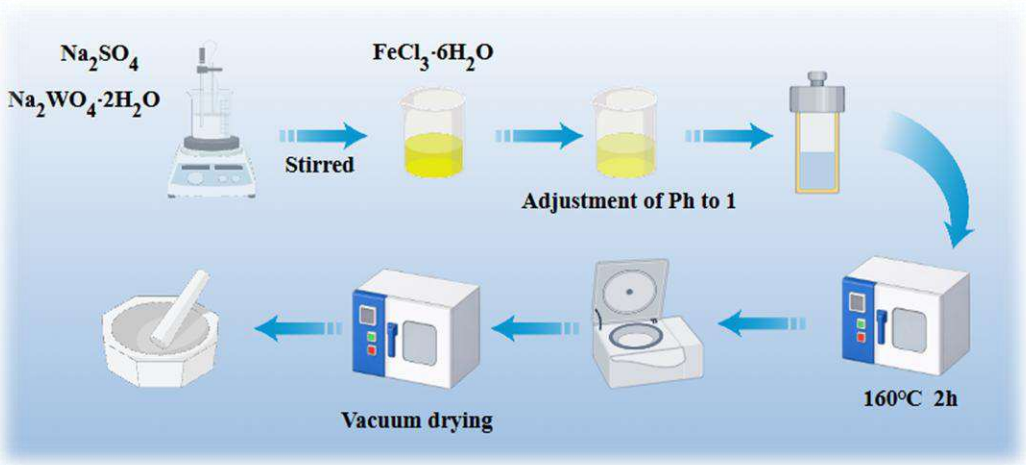


Fig.1 Preparation Flow Chart of WO_3

2.1.2 Synthesis of $BiVO_4$

As shown in **Fig. 2,**a certain amount of bismuth nitrate pentahydrate was dissolved in 30 mL of deionized water containing 3 mL of nitric acid solution under vigorous stirring for 30 min to obtain solution A. Meanwhile, an appropriate amount of ammonium metavanadate was dissolved in 30 mL of deionized water with 1 mL of ethylenediamine solution under stirring until complete dissolution, denoted as solution B. Under magnetic stirring, solution B was added dropwise to solution A to form a uniform yellow suspension. The suspension was vigorously stirred at room temperature for 3 h, and then transferred into a 100 mL Teflon-lined autoclave and heated at 160 °C for 16 h. After the reaction, the mixture was naturally cooled to room temperature. The yellow precipitate was collected by centrifugation and washed alternately with anhydrous ethanol and deionized water until

the supernatant was neutral. Finally, the product was dried in an oven at 80 °C for 12 h.

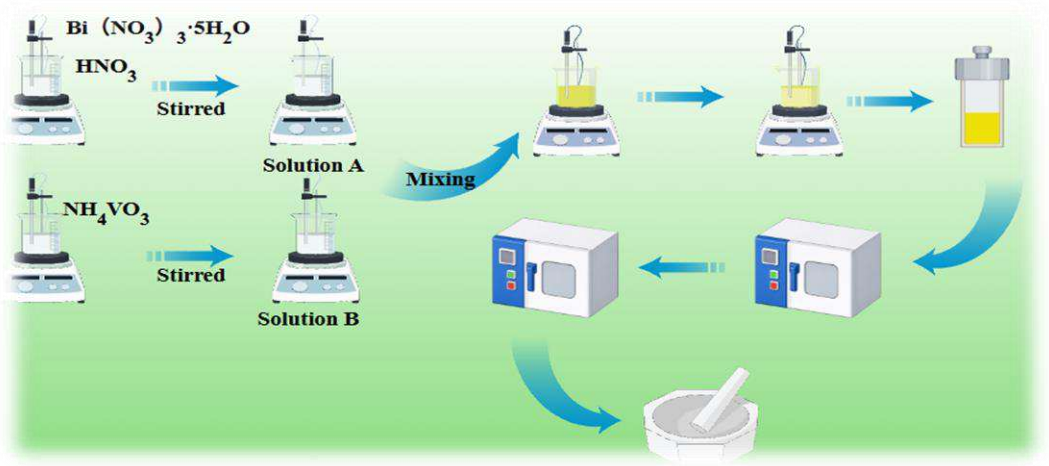


Fig.2 Preparation Flow Chart of $BiVO_4$

2.2 Material characterization

The crystal structure of the samples was analyzed by X-ray diffraction (XRD, Bruker D8 Advance) using Cu Kα radiation (λ = 0.15406 nm). The morphology was observed with a TESCAN MIRA4 field-emission scanning electron microscope (SEM). The microstructure of the catalyst was investigated by high-resolution transmission electron microscopy (HRTEM, JEM-1200EX). The surface chemical states and band positions were examined by X-ray photoelectron spectroscopy (XPS, PHI-5702). Fourier-transform infrared (FT-IR) spectra were recorded on a Nexus 670 spectrometer in the wavenumber range of 400–4000 cm^{-1} to analyze the chemical bonds and functional groups. The optical absorption properties were measured

by ultraviolet-visible diffuse reflectance spectroscopy (UV–Vis DRS, TU-1901) in the wavelength range of 200–800 nm. Photoluminescence (PL) spectra were recorded on an RF-6000 fluorescence spectrometer at an excitation wavelength of 480 nm. More detailed experimental parameters are provided in the Supporting Information.

2.3 Photo-Fenton degradation experiments

The photo-Fenton performance of the samples was evaluated using 50 mg/L tetracycline (TC) aqueous solution at room temperature (25 °C). The pH of the solution was adjusted with hydrochloric acid and sodium hydroxide. Typically, 20 mg of catalyst was added into 100 mL of TC solution and stirred in the dark for 30 min to reach adsorption–desorption equilibrium. Then, a certain amount of hydrogen peroxide was added into the system. A 300 W xenon lamp (VS-GCH-XE-300) was used as the simulated solar light source, placed 15 cm above the suspension. At 10 min intervals, 3 mL of suspension was withdrawn and centrifuged. The concentration of TC was determined by measuring the absorbance at 356 nm with a UV-Vis spectrophotometer.

The TC removal efficiency was calculated as follows:

$$\frac{(C_0 - C_t)}{C_0} \times 100\% = \frac{(A_0 - A_t)}{A_0} \times 100\%$$

Where C_t and C_0 are the TC concentrations at time t and the initial state, respectively; A_t and A_0 are the corresponding absorbance values.To

identify the reactive species involved in the photo-Fenton process, radical scavenging experiments were carried out under identical reaction conditions. Specifically, 5 mL of isopropanol (IPA), 0.1 mM 1,4-benzoquinone (BQ) and 0.1 mM ammonium oxalate (IA) were used as scavengers for hydroxyl radicals (·OH), superoxide radicals ($\cdot O_2^-$) and holes (h^+), respectively.

2.4 Photoelectrochemical measurements

Electrochemical impedance spectroscopy (EIS) and transient photocurrent tests were performed on a three-electrode electrochemical workstation (CorrTest CS350) with 0.1 M Na_2SO_4 as the electrolyte. For the preparation of the working electrode, 15 mg of sample and 2 mg of acetylene black were dispersed in a mixed solution of N-methyl-2-pyrrolidone (NMP) and polyvinylpyrrolidone (PVP), and then coated onto an indium tin oxide (ITO) glass substrate followed by drying. A platinum sheet was used as the counter electrode, and a saturated calomel electrode (SCE) served as the reference electrode.

3. Results and Discussion

3.1 Structural and compositional characterization

The crystal phase structure of the catalysts was analyzed by XRD. As shown in Fig.3a, the diffraction peaks at the (020), (111), (220) and (310) planes of the nanosphere sample are consistent with those of

$WO_3 \cdot 0.33H_2O$ (JCPDS No. 35-0270). The sharp and well-defined peaks without impurity signals indicate the high purity and good crystallinity of the $WO_3 \cdot 0.33H_2O$ sample. The diffraction peaks of $BiVO_4$ match well with the standard card (PDF #14-0688), and no obvious impurity peaks are observed, confirming the high purity and good crystallinity of the as-prepared $BiVO_4$. The characteristic diffraction peaks of pure $BiVO_4$ appear at $2\theta = 28.8°$, 30.5°, 34.5°, 35.2°, 39.8°, 42.5°, 46.7° and 47.3°, corresponding to the (121), (040), (200), (002), (211), (051), (240) and (042) crystal planes of monoclinic scheelite $BiVO_4$, respectively[18-19].

As shown in Fig.3b, with the increase of Fe doping content, the diffraction peaks shift slightly. The shift is very weak due to the similar ionic radii of Fe^{3+} and W^{6+}, but it still verifies that Fe ions are successfully incorporated into the WO_3 lattice without the formation of secondary phases[20]. For the composite samples, the characteristic peaks of $BiVO_4$ at $2\theta \approx 28.8°$ and 30.5° (corresponding to the (121) and (040) planes) are clearly observed, which are consistent with the standard card (PDF #77-0097)[15]. With the increase of $BiVO_4$ content, the intensity of these peaks gradually increases. Notably, the peak positions of Fe-doped WO_3 remain almost unchanged after the formation of the composite, indicating that the introduction of $BiVO_4$

does not cause obvious lattice distortion of Fe-doped WO_3.

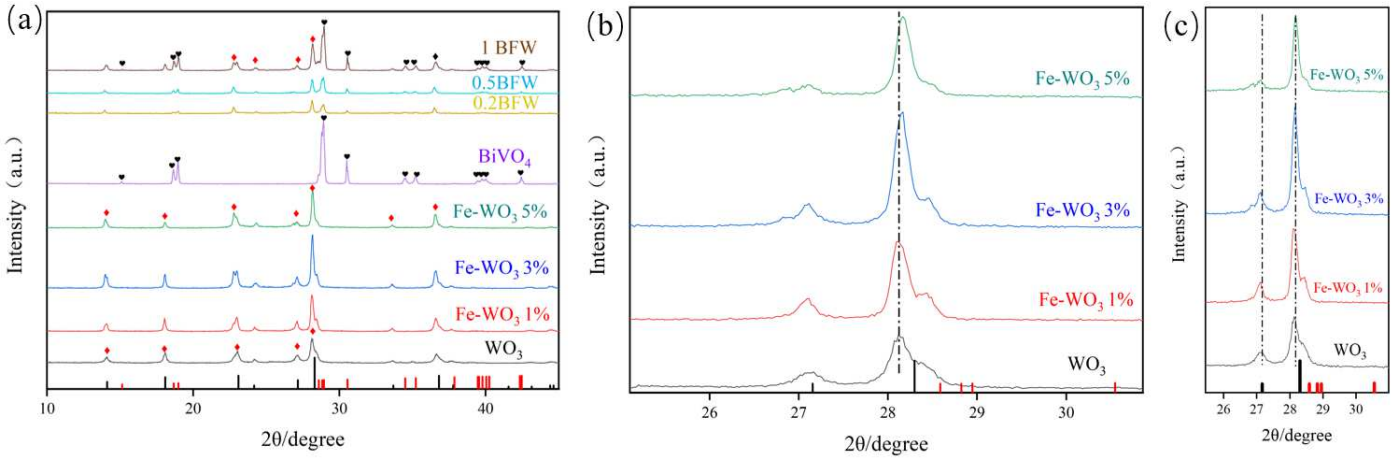


Fig.3XRD patterns of pristine WO_3, pure $BiVO_4$, Fe-doped WO_3 and Fe-WO_3/$BiVO_4$ composite samples

To further verify the composition of the composites, FT-IR characterization was performed (Fig4). In the FT-IR spectra, the broad absorption band in the range of 2900–3400 cm^{-1} is attributed to O–H stretching vibration, and the peak at 1607.4 cm^{-1} corresponds to the H–O–H bending vibration of adsorbed water. The characteristic bands of WO_3 in the 400–1200 cm^{-1} region are assigned to the W–O–W bridging vibration mode in the corner-sharing octahedral structure. All Fe-doped WO_3 samples retain the characteristic O–W–O vibration peaks of WO_3, indicating that Fe doping does not destroy the main crystal structure of WO_3.

The composite samples simultaneously exhibit the characteristic peaks of W–O–W from WO_3 and the V–O, Bi–O, V–O–Bi vibration

peaks from $BiVO_4$, confirming the coexistence of both phases and the successful preparation of the two-component composite catalyst. Notably, the characteristic peaks in the 400–1200 cm^{-1} region show slight shifts and peak broadening, suggesting that there are strong chemical interactions and electronic coupling at the interface between $BiVO_4$ and Fe-WO_3, rather than simple physical mixing.

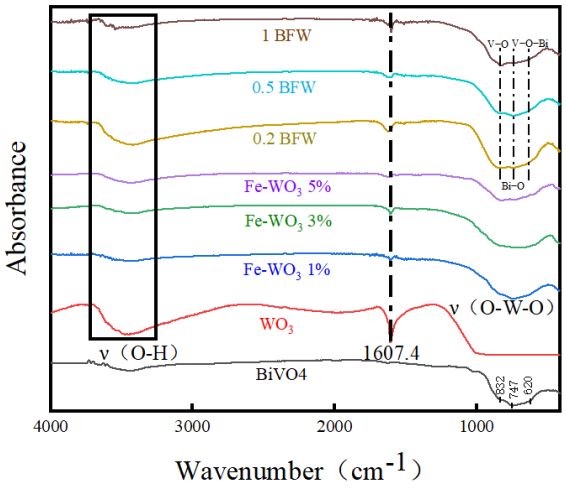


Fig.4 FT-IR spectra of pristine WO_3, pure $BiVO_4$, Fe-doped WO_3 and Fe-WO_3/$BiVO_4$ composite samples

3.2 Morphology and microstructure analysis

Fig.5a shows that pristine WO_3 exhibits a typical hierarchical microsphere morphology with a diameter of 2–3 μm, which is assembled from numerous nanocrystallites. The rough surface with granular protrusions endows the material with a high specific surface area foundation.

As shown in **Fig.5b**, pure $BiVO_4$ presents a uniform tetragonal

prismatic structure with a particle size of approximately 1 μm. The smooth surface and well-defined edges indicate the high crystallinity and favorable dispersibility of the as-prepared $BiVO_4$.

After 3% Fe doping (**Fig.5c**), the sample maintains the intact microsphere framework, while the building units evolve from granular aggregates to radially assembled two-dimensional nanosheets, forming a flower-like hierarchical structure. The nanosheets with clear edges grow outward from the center of the microspheres. This morphology evolution induced by Fe doping is consistent with previous reports, and the flower-like architecture assembled by nanosheets can provide more surface active sites and mass diffusion channels for reactants[21][22].

Fig.5d presents the SEM image of the 0.5 Fe-WO_3/$BiVO_4$ composite. The sample retains the microsphere morphology with a slightly reduced particle size, and the surface shows an interwoven structure of nanosheets and nanoparticles. The two phases are in close contact at the interface without obvious macroscopic phase separation or particle agglomeration. Such an intimate heterojunction interface provides a structural foundation for the rapid separation and transfer of photogenerated charge carriers, which is a key morphological feature for enhancing photocatalytic performance.

Transmission electron microscopy (TEM) images (**Fig.5e–3f**) are

consistent with the SEM observations. The low-magnification TEM image (**Fig.5e**) reveals that the composite maintains the hierarchical flower-like microsphere structure with a diameter of 2–3 μm, which is constructed by two-dimensional nanosheets. The rough surface and abundant hierarchical pore structure on the flower-like microspheres can provide sufficient active sites for the photocatalytic reaction, which is in good agreement with the SEM results. In the magnified TEM image (**Fig.5f**), an obvious contrast difference can be observed at the edge of the $BiVO_4$ microsphere, with a modification layer of about ten nanometers in thickness uniformly coated on the surface, confirming the nanoscale integration of WO_3 on the $BiVO_4$ support.

The HRTEM image (**Fig.5g**) clearly shows the crystalline interface between Fe-doped WO_3 and $BiVO_4$. The lattice fringes in region ① are well-defined and periodic, with an interplanar spacing of 0.308 nm, which is consistent with the (121) crystal plane of monoclinic scheelite $BiVO_4$. The lattice fringes in region ② correspond to an interplanar spacing of 0.367 nm, assignable to the (200) plane of monoclinic WO_3. Compared with the standard interplanar spacing (0.365 nm) of pure WO_3, the measured value shows a slight increase. This phenomenon arises from the substitution of smaller W^{6+} (six-coordinate radius 0.60 Å) by larger Fe^{3+} (six-coordinate radius 0.645 Å)

in the lattice, which induces local lattice expansion and provides microstructural evidence for the successful incorporation of Fe into the WO_3 lattice[23].

Further observation of the two-phase contact area reveals a clear and continuous crystalline interface between $BiVO_4$ and Fe-WO_3, without an obvious amorphous interlayer or physical gap. This result indicates that the two phases form a tightly bonded heterojunction rather than a simple physical mixture. Such a structure can effectively reduce the interfacial charge transfer resistance and provide unobstructed pathways for the separation and migration of photogenerated carriers, which plays a critical role in improving the photocatalytic performance of the composite.

To further verify the compositional uniformity of the composite microspheres, EDS mapping characterization was performed, as shown in **Fig.5h–l**. The five characteristic elements (Bi, W, V, O, and Fe) are uniformly distributed throughout the microsphere. The distribution ranges of Bi and V are highly consistent, corresponding to the uniform loading of the $BiVO_4$ phase. The co-distribution of W and Fe confirms that Fe is homogeneously doped into the WO_3 matrix without local aggregation. Oxygen, as a common component of the two oxides, is distributed across the entire microsphere structure. The uniform

distribution of all elements demonstrates that Fe-WO_3 and $BiVO_4$ are uniformly composited rather than simply physically mixed, which provides a structural guarantee for the sufficient construction of heterojunctions and the stable improvement of photocatalytic performance.

Fig.5m shows the fast Fourier transform (FFT) pattern corresponding to the two-phase interface region of the Fe-WO_3/$BiVO_4$ composite. Two sets of independent single-crystal diffraction lattices can be clearly distinguished, indicating that both phases in the selected microregion have good crystallinity without obvious amorphous diffuse features. The set of diffraction spots near the central spot corresponds to an interplanar spacing of 0.386 nm, which is assigned to the (002) plane of monoclinic WO_3; the other set of spots farther from the center corresponds to a spacing of 0.198 nm, which matches well with the (231) plane of monoclinic scheelite $BiVO_4$. Compared with the standard value of pure WO_3 (0.384 nm), the measured interplanar spacing is slightly larger, which is consistent with the HRTEM results and further confirms the local lattice expansion induced by Fe^{3+} doping from the diffraction perspective. This result verifies that WO_3 and $BiVO_4$ form a tightly bonded crystalline heterojunction at the nanoscale rather than a simple physical blend, and provides a smooth transmission channel for the

cross-interface separation and migration of photogenerated carriers.

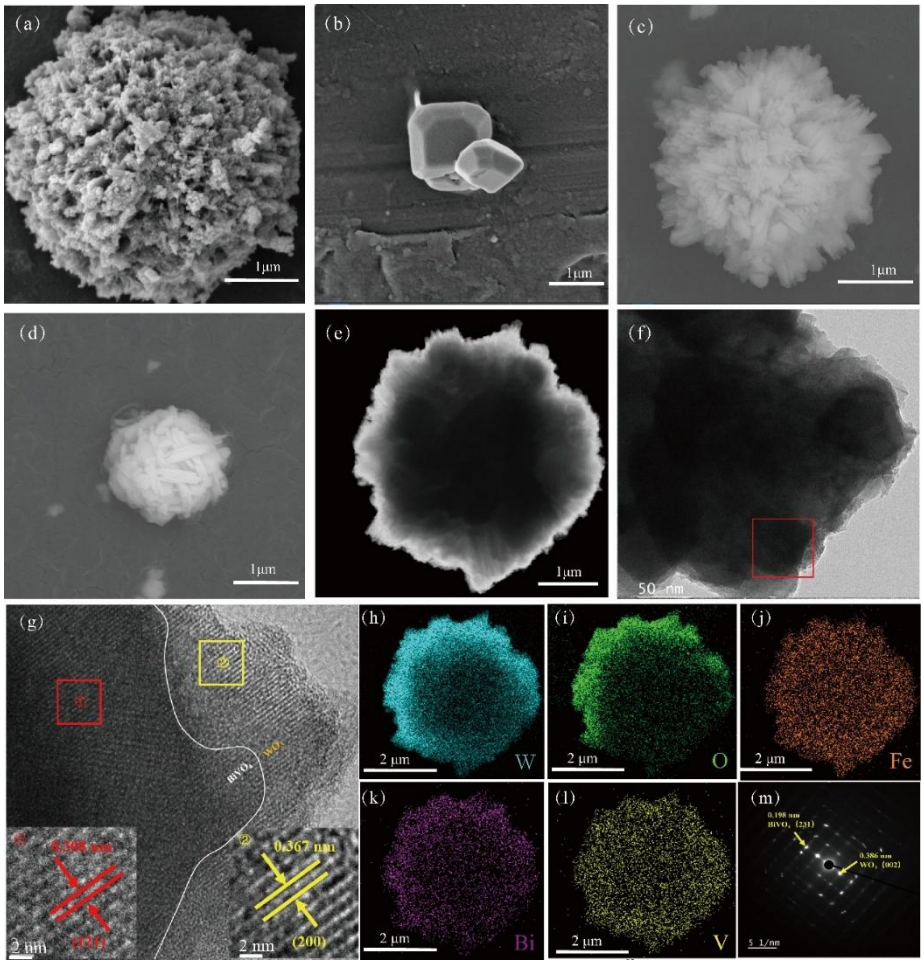


Fig. 5 SEM images of (a) WO_3, (b) $BiVO_4$, (c) 3% Fe-WO_3, (d) 0.5 Fe-WO_3/$BiVO_4$; (e–g) HRTEM images, (h–l) EDS elemental mappings, (m) FFT pattern of 0.5 Fe-WO_3/$BiVO_4$.

XPS measurement was carried out on the 0.5 Fe-WO_3/$BiVO_4$ composite to investigate the elemental composition and chemical valence states. **Fig.6a** shows the survey spectrum of the composite, in which characteristic peaks of W 4f, O 1s, V 2p, C 1s, Fe 2p, and Bi 4f are clearly observed, confirming the coexistence of W, O, V, C, Fe, and Bi elements in the composite.

Fig.6b displays the high-resolution W 4f XPS spectrum. Two characteristic peaks located at 35.62 eV and 37.81 eV are attributed to W $4f_{7/2}$ and W $4f_{5/2}$, respectively, which is consistent with the reported values of W^{6+} in the WO_3 lattice[24][25], indicating that tungsten exists in the +6 oxidation state in the composite.

Fig.6c shows the high-resolution O 1s spectrum, which can be deconvoluted into two components. The main peak at 530.40 eV corresponds to lattice oxygen in W–O, Bi–O, V–O, and Fe–O bonds, confirming the integrity of the crystal framework. The shoulder peak at 532.52 eV is ascribed to defective oxygen species including surface oxygen vacancies, hydroxyl groups, and adsorbed oxygen. The introduction of Fe^{3+} doping and the lattice distortion at the heterojunction interface jointly promote the formation of oxygen vacancies, which can effectively facilitate the separation of photogenerated carriers.

In the high-resolution Bi 4f spectrum (**Fig.6d**), two peaks at 159.14 eV and 164.43 eV are assigned to Bi $4f_{7/2}$ and Bi $4f_{5/2}$, respectively. The binding energies show a slight positive shift compared with those of pure $BiVO_4$, which is attributed to electron transfer at the heterojunction interface[26,27].

The high-resolution V 2p spectrum (**Fig.6e**) exhibits two peaks at

516.66 eV and 523.87 eV, corresponding to V $2p_{3/2}$ and V $2p_{1/2}$, respectively, indicating that vanadium is in the +5 oxidation state (V^{5+}). The shift direction of V 2p is consistent with that of Bi 4f, further verifying that the $BiVO_4$ phase experiences overall electron depletion, which is a typical manifestation of charge transfer driven by the built-in electric field at the heterojunction interface[26][28].

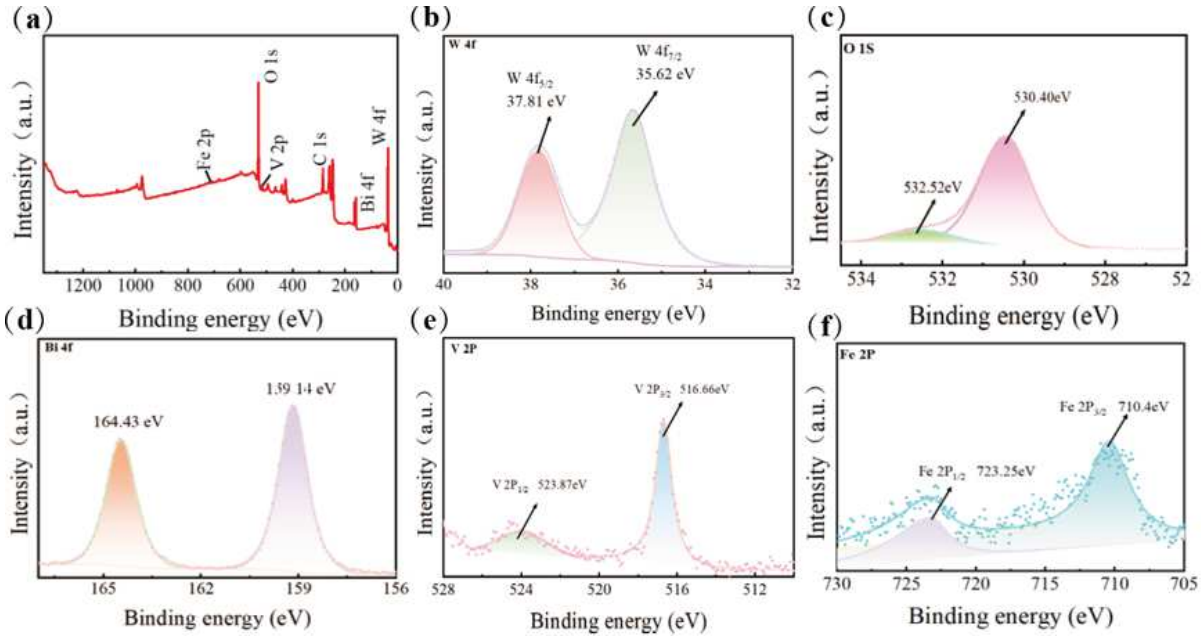


Fig.6 (a) Survey spectrum and high-resolution XPS spectra of (b) W 4f, (c) O 1s, (d) Bi 4f, (e) V 2p, and (f) Fe 2p for the 0.5 Fe-WO_3/$BiVO_4$ composite.

Fig.6f presents the high-resolution Fe 2p spectrum. Characteristic peaks appear at 710.4 eV and 723.25 eV, corresponding to Fe $2p_{3/2}$ and Fe $2p_{1/2}$, respectively. Notably, the binding energy of Fe $2p_{3/2}$ shifts by approximately 0.8 eV toward lower energy compared with the reported value for pure Fe_2O_3, which is consistent with the reported offset for

lattice-doped Fe species[29]. This result indicates that Fe is mainly present as Fe^{3+} doped into the WO_3 lattice without detectable impurity phases[30]. Overall, the XPS results demonstrate that all elements in the 0.5 Fe-WO_3/$BiVO_4$ composite are in the expected oxidation states, further confirming the successful construction of the two-phase heterojunction and the stable surface chemical state of the material.

3.3 Photoelectrochemical and optical properties

To elucidate the regulatory effects of Fe doping and heterojunction construction on the photoelectrochemical performance of the materials, UV–vis absorption spectroscopy, photoluminescence spectroscopy, electrochemical impedance spectroscopy and transient photocurrent tests were systematically performed to evaluate the light response[31], carrier separation efficiency and interfacial transport properties of the samples, as shown in **Fig.7**.

Fig.7a shows the UV–vis absorption spectra of different samples. Pristine WO_3 mainly absorbs light in the ultraviolet and near-visible region with an absorption edge at approximately 460 nm. After Fe doping, the absorption intensity in the visible region is enhanced to different degrees, and the absorption edge is slightly red-shifted. The sample with 3% Fe doping exhibits the optimal visible-light absorption performance, which is attributed to the impurity levels introduced by

Fe^{3+} doping that narrow the band gap and broaden the light response range. After coupling with $BiVO_4$, the absorption edge of the BFW series samples further shifts to longer wavelengths, indicating that the 0.5 BFW composite has a stronger visible-light utilization capacity.

Photoluminescence (PL) spectroscopy can intuitively reflect the recombination degree of photogenerated electron–hole pairs[32]; a lower fluorescence intensity corresponds to a higher carrier separation efficiency. As shown in **Fig.7b**, both pure WO_3 and pure $BiVO_4$ exhibit strong PL emission peaks, indicating severe photogenerated carrier recombination in single-phase materials. After Fe doping, the PL intensity of WO_3 decreases to varying degrees, suggesting that doping defects can act as charge trapping sites and suppress carrier recombination to a certain extent. After constructing the heterojunction, the PL intensity of the BFW series samples further decreases, and the 0.5 BFW sample shows the lowest fluorescence intensity, demonstrating that it has the most efficient photogenerated carrier migration and the lowest recombination rate.

Electrochemical impedance spectroscopy (EIS) is used to analyze the charge transfer behavior at the catalyst interface and evaluate the charge transport performance[33]. **Fig.7c** shows the Nyquist plots of pure WO_3 and the 0.5 BFW composite. The arc radius of the 0.5 BFW

electrode is significantly smaller than that of pure WO_3, indicating that the composite has lower charge transfer resistance and faster electron–hole separation kinetics.

Fig.7d presents the transient photocurrent response curves of the samples under multiple on–off light cycles. All samples generate photocurrent rapidly when light is turned on and return to the dark current level quickly when light is turned off, showing good photoresponse reversibility. The photocurrent densities of pure WO_3 and pure $BiVO_4$ are relatively low, while the 0.5 BFW composite exhibits a significantly higher photocurrent density, which is consistent with the PL and EIS results and confirms that the heterojunction effectively improves the separation and utilization efficiency of photogenerated carriers. Moreover, the photocurrent density shows no obvious attenuation after four cycles, indicating that the composite has excellent photoelectrochemical stability.

In summary, the synergistic effect of Fe doping and $BiVO_4$ heterojunction construction can simultaneously broaden the light response range, suppress carrier recombination, and reduce the interfacial charge transfer resistance, ultimately achieving a cooperative enhancement of the catalytic performance.

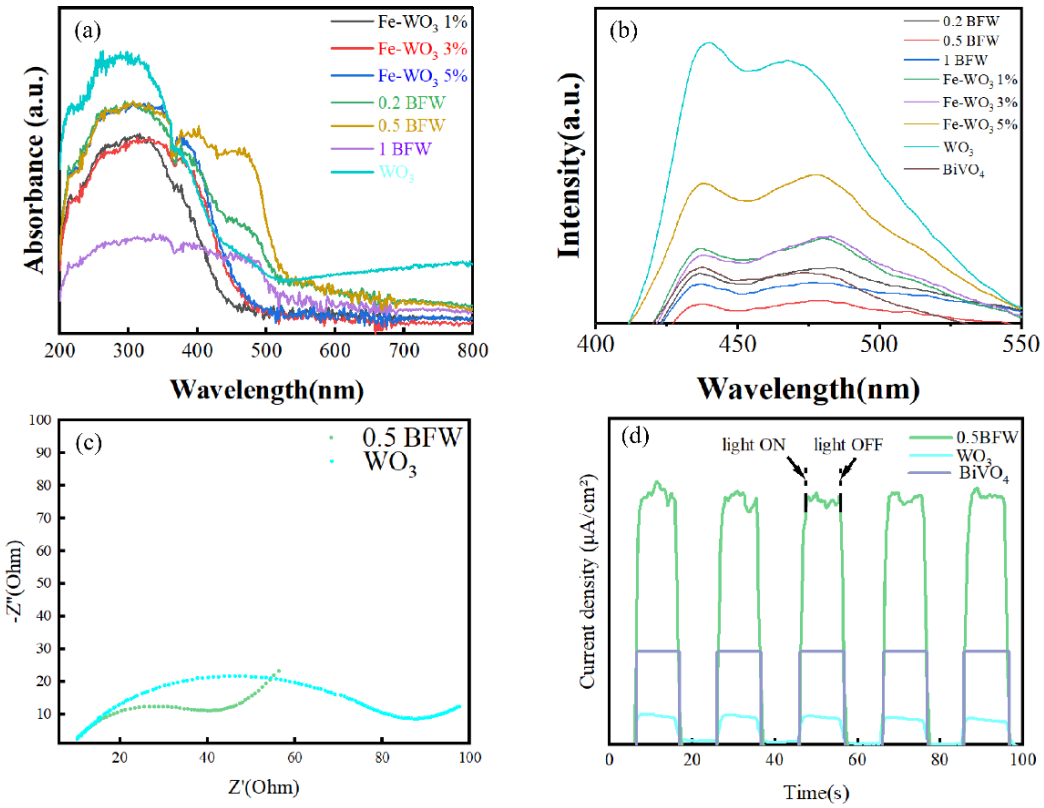


Fig.7(a) UV–Vis absorption spectra; (b) PL spectra; (c) EIS Nyquist plots; (d) transient photocurrent responses.

3.4 Photo-Fenton degradation performance

The photocatalytic and photo-Fenton activities of the samples were evaluated using 100 mL of 50 mg/L tetracycline (TC) solution as the target pollutant with a catalyst dosage of 0.2 g/L. After 30 min of dark stirring to reach the adsorption–desorption equilibrium, the degradation experiments were conducted under irradiation from a 300 W xenon lamp as simulated sunlight. At predetermined time intervals, 3 mL of the suspension was withdrawn and centrifuged to remove the

catalyst, and the TC concentration was determined using a UV-759 UV–vis spectrophotometer. The TC removal efficiency was calculated based on the ratio of[34-35]:

$$\eta = \frac{(C_0 - C_t)}{C_0} \times 100\%.$$

Fig8.a shows the photocatalytic degradation performance without H_2O_2 addition. During the dark adsorption stage (−30 to 0 min), the adsorption capacity varies among different samples, and the composite samples generally exhibit higher adsorption capacity than the single-phase materials, which is likely due to the morphology evolution of WO_3 induced by Fe doping. Under light irradiation (0 to 60 min), all samples can degrade TC to varying degrees, but the overall removal efficiency is limited in the absence of H_2O_2.

Fig.8.b presents the photo-Fenton degradation performance with H_2O_2 addition. Notably, within the first 10 min of light irradiation, the TC removal efficiencies of 0.2 BFW, 0.5 BFW and 1 BFW reach 65.3%, 76.8% and 61.3%, respectively, which are superior to those of the single-phase Fe-doped WO_3 samples. The results demonstrate that the introduction of $BiVO_4$ positively enhances the photo-Fenton performance of Fe-doped WO_3. Compared with pristine WO_3, the Fe-doped samples show significantly improved degradation efficiency under photo-Fenton conditions, reflecting the synergistic promotion of

ion doping and the Fenton reaction. The further enhanced degradation efficiency of the composite samples verifies the crucial role of the heterojunction structure in the photo-Fenton process. In the control group with only H_2O_2 and light, the TC removal rate is only 12.5% after 60 min, indicating that H_2O_2 alone cannot achieve efficient pollutant removal. In addition, the TC removal rate is less than 10% under direct light irradiation without catalyst, excluding the contribution of direct photolysis of TC under the experimental conditions.

To further quantify the degradation kinetics, the pseudo-first-order kinetic model was applied to fit the reaction process. As shown in **Fig.8c**, the apparent rate constants Kobs of WO_3, $BiVO_4$, Fe-WO_3 1%, Fe-WO_3 3%, Fe-WO_3 5%, 0.2 BFW, 0.5 BFW and 1 BFW are 0.0031 min^{-1}, 0.0033 min^{-1}, 0.0164 min^{-1}, 0.0184 min^{-1}, 0.0177 min^{-1}, 0.0176 min^{-1}, 0.0215 min^{-1} and 0.0125 min^{-1}, respectively. The 0.5 BFW sample possesses the highest degradation rate constant, which is 7 times that of pure WO_3 and 1.35 times that of the single Fe-doped system, further confirming the synergistic enhancement of ion doping and heterojunction construction on the photo-Fenton performance.

The effects of key operating parameters on the degradation performance were systematically investigated, and the results are shown in **Fig.8d–f**. In the dark adsorption stage, all samples reach

adsorption–desorption equilibrium within 30 min, and the adsorption capacity increases slightly with the increase of catalyst dosage. Under light irradiation, the blank group without catalyst shows almost no TC concentration change, indicating that the direct photolysis of TC can be neglected. With the catalyst dosage increasing from 0.1 g/L to 0.2 g/L, the degradation efficiency is significantly improved, as more surface active sites and photogenerated carriers are available for the reaction. However, when the dosage further increases to 0.4 g/L, the degradation efficiency decreases slightly, which is caused by the light scattering and shielding effect of excessive particles, reducing the visible light utilization efficiency of the system[36].

Fig.8e illustrates the effect of initial pH on the photo-Fenton degradation performance in the range of pH 3–11. The catalyst maintains high degradation activity under acidic and neutral conditions; the TC removal rates at pH 3, 5 and 7 are 92.1%, 94.5% and 92.0%, respectively. Under alkaline conditions (pH 9 and 11), the removal efficiency decreases to a certain extent but still remains above 78%, showing a relatively wide pH application range. The performance decline under strong alkaline conditions is related to the change of TC molecular charge state and the reduced stability of partial reactive species[35].

Fig.8f shows the effect of H_2O_2 concentration on TC degradation. The removal rates at H_2O_2 concentrations of 0, 1, 3 and 6 mM are 51%, 84%, 93% and 87.5%, respectively. Without H_2O_2, the removal efficiency is only about 50%, confirming the synergistic effect of H_2O_2 and the catalyst. The degradation efficiency first increases with the rise of H_2O_2 concentration and reaches the maximum at 3 mM, then shows a downward trend. The performance attenuation at excessive H_2O_2 concentration is attributed to the quenching effect of redundant H_2O_2 on active radicals, which weakens the overall oxidation capacity of the system[38].

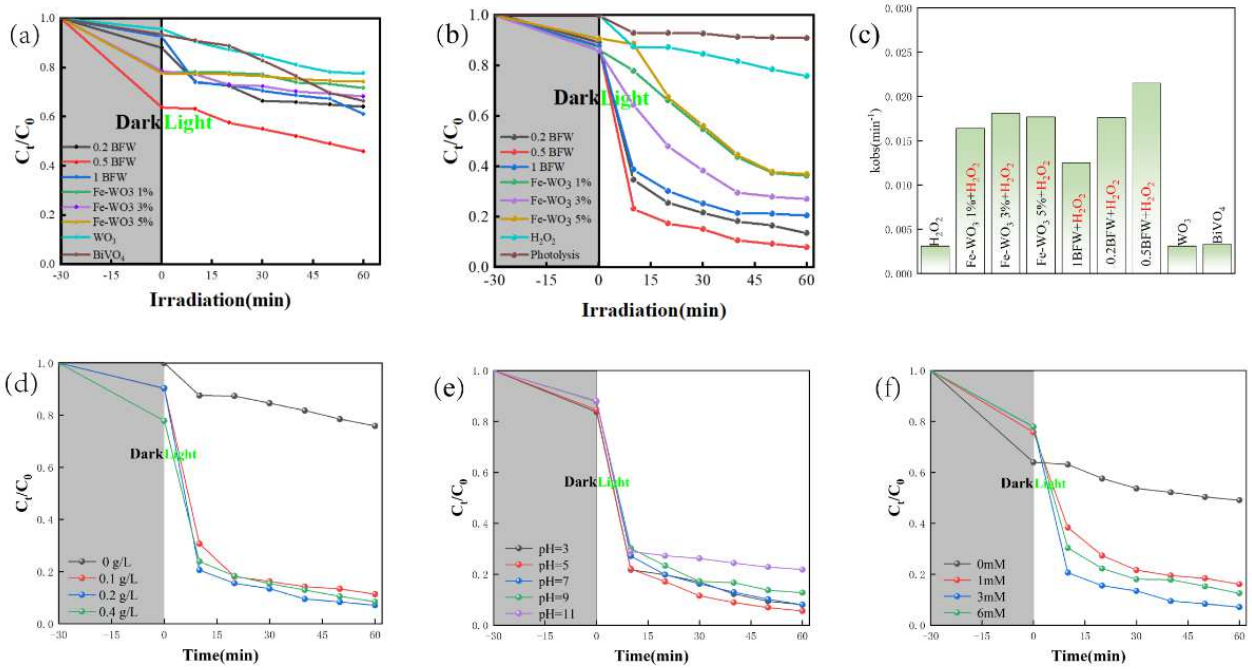


Fig.8(a) Photocatalytic degradation curves; (b) photo-Fenton degradation curves; (c) apparent rate constants; (d–f) effects of

catalyst dosage, initial pH and H_2O_2 concentration on degradation performance.

3.5 Reactive species identification and cycling stability

Radical scavenging experiments were conducted to identify the dominant reactive oxygen species in the photo-Fenton system, with the results shown in Figures 7a and 7b. After the addition of BQ ($\cdot O_2^-$ scavenger), the TC removal efficiency drops to 72.3%, and the apparent rate constant decreases to 5.926×10^{-4} min^{-1}, demonstrating that $\cdot O_2^-$ is the predominant reactive species in the degradation process. The addition of IPA (·OH scavenger) and IA (h^+ scavenger) also reduces the degradation efficiency to different degrees, indicating that ·OH and h^+ also participate in the TC degradation process as auxiliary active species.

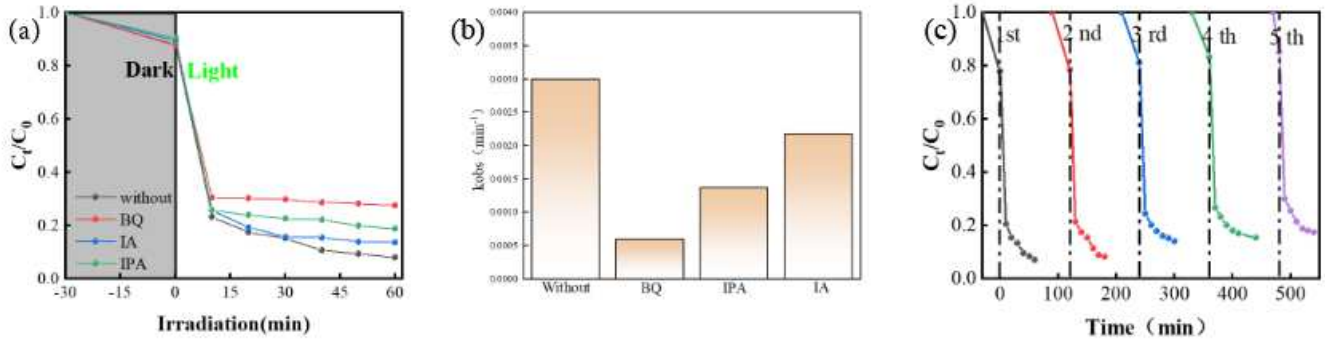


Fig.9(a) Radical scavenging experiments; (b) corresponding apparent rate constants; (c) cycling stability test

The reusability of the 0.5 BFW catalyst was evaluated by five

consecutive cycle experiments. As shown in Figure 7c, the TC removal rate decreases from 92.9% to 82.6% after five cycles, with no obvious performance decay, indicating that the composite catalyst possesses excellent structural stability and catalytic durability.

3.6 Response surface methodology optimization

Response surface methodology (RSM) was employed to optimize the photo-Fenton reaction system under alkaline conditions. Catalyst dosage (X_1), initial pH (X_2) and H_2O_2 concentration (X_3) were selected as independent variables, and the ratio C_{60}/C_0 was taken as the response value to construct a quadratic regression prediction model. The experimental design and parameter ranges are listed in **Table 1**. A total of 17 groups of experiments were conducted (**Table 2**), and the second-order polynomial regression equation was obtained as follows:

$$Y = 1.68414 - 5.74745X_1 - 0.142717X_2 - 0.248357X_3 + 0.088053X_1X_2 - 0.200787X_1X_3 + 0.010472X_2X_3 + 10.41307X_1^2 + 0.007329X_2^2 + 0.026355X_3^2$$

Three-dimensional response surface plots were used to analyze the interactive effects of the three factors on TC degradation performance under alkaline conditions, as shown in **Fig.10**.

Fig.10a presents the response surface of catalyst dosage and initial pH at a fixed H_2O_2 concentration. With the simultaneous increase of

catalyst dosage and pH, the normalized TC concentration C_t/C_0 first decreases and then increases, corresponding to a trend of first increasing and then decreasing in degradation efficiency. This parabolic trend is attributed to the threshold effect of both factors: excessive catalyst loading causes light scattering and particle shielding, reducing the visible light utilization efficiency, while excessively strong alkaline conditions inhibit the generation and stability of reactive species and deactivate iron active sites, ultimately weakening the degradation performance.

Fig.10b.c show the response surfaces at fixed initial pH and fixed catalyst dosage, respectively, and their overall trends are consistent with **Fig.10a. b** reveals a significant interaction between catalyst dosage and H_2O_2 concentration: a moderate increase in H_2O_2 concentration provides more precursors for reactive species generation and enhances degradation, while excess H_2O_2 scavenges ·OH through side reactions and reduces the degradation efficiency. Figure 8c shows a synergistic effect between pH and H_2O_2 concentration; the lowest C_t/C_0 is achieved when both factors are within their optimal ranges, and deviation of either parameter impairs the degradation performance.

Based on the regression model, the optimal reaction parameters at pH 11 were predicted: catalyst dosage of 0.264 g/L and H_2O_2

concentration of 3.53 mM, with a predicted TC removal efficiency of 86.3%. Three parallel verification experiments were performed under the optimal conditions, and the average removal efficiency was 82.1%. The small deviation between the experimental value and the predicted value confirms that the model has good fitting accuracy and can reliably predict the degradation performance of the system.

Table 1 Experimental ranges and levels of independent variables for the photo-Fenton process

Symbol X_i	Independent variable	Range and level		
		Low (-1)	Center (0)	High (1)
X_1	催化剂浓度（g/L）	0	0.2	0.4
X_2	pH	3	7	11
X_3	H_2O_2（mL）	0	3	6

Table 2 Experimental design of response surface methodology (RSM)

Run	X_1（Catalyst dosage）	X_2（pH）	X_3（H_2O_2）	$Y(C_{60}/C_0)$
1	0.2	7	3	0.02648
2	0.4	3	3	0.06118
3	0.4	7	0	0.70531
4	0.2	7	3	0.02538
5	0.2	3	6	0.08274
6	0.2	7	3	0.02583
7	0.2	3	0	0.6734
8	0.4	11	3	0.33971
9	0	7	6	0.89532
10	0	3	3	0.921
11	0.4	7	6	0.11874
12	0.2	11	6	0.3391
13	0	7	0	1
14	0.2	7	3	0.02643
15	0.2	7	3	0.0265
16	0	11	3	0.91776
17	0.2	11	0	0.4271

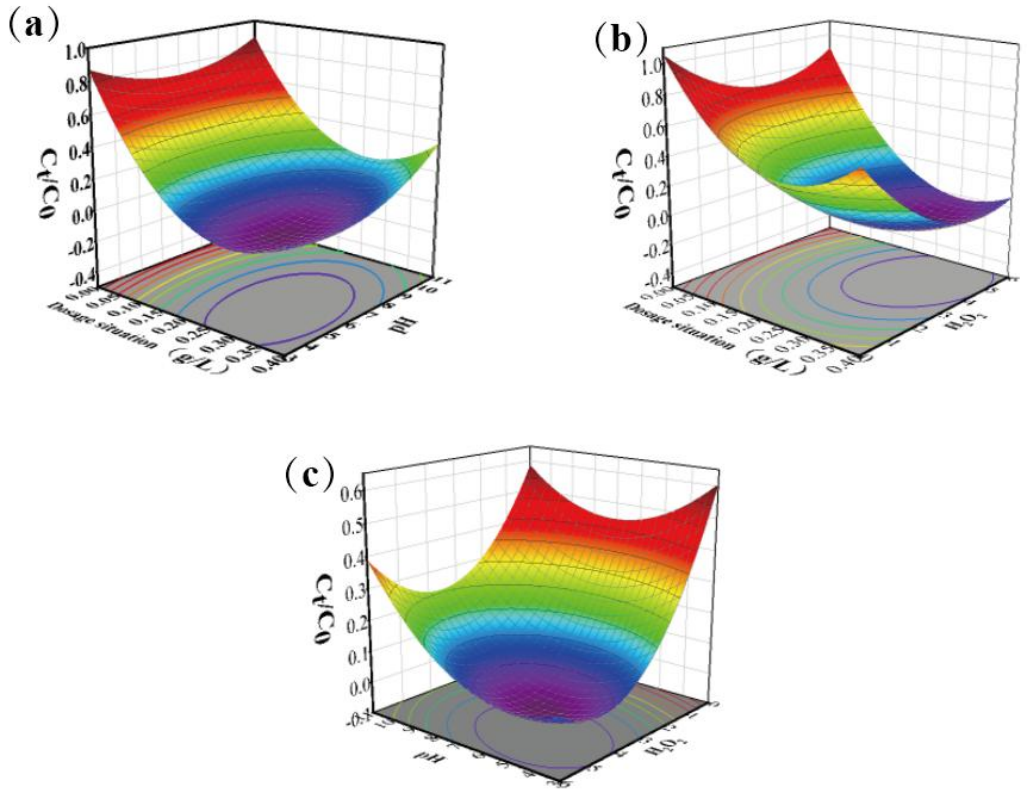


Fig.10 3D surface plots: (a) Solution pH and dosage; (b) Dosage and H_2O_2 concentration; (c) H_2O_2 concentration and solution pH

3.5 Degradation mechanism analysis

The optical band gaps of the samples were calculated by the Tauc plot method. The results show that pristine WO_3 has a band gap of 2.93 eV, with light absorption mainly concentrated in the ultraviolet and near-visible region. After Fe doping, Fe^{3+} substitutes W^{6+} in the WO_3 lattice and introduces impurity levels in the band gap, which reduces the energy required for electron transition. Accordingly, the band gaps of Fe-WO_3 samples are narrowed to different degrees; the 3% Fe-WO_3

sample has a band gap of 2.81 eV, with an obviously expanded visible light response range. After coupling with narrow-band-gap $BiVO_4$, the absorption edges of BFW composite samples further red-shift to longer wavelengths, and the band gap of 0.5 BFW is reduced to 2.40 eV. The continuous narrowing of the band gap enables the composite to capture more visible photons and generate more photogenerated electron–hole pairs, providing sufficient charge carriers for the subsequent catalytic reaction.

The valence band (VB) and conduction band (CB) edge potentials of the semiconductors were calculated by the empirical formula based on Mulliken electronegativity: $E_{VB}=X-E^e+0.5E_g$、$E_{CB}=E_{VB}-E_g$[37,38]

where E_{VB} and E_{CB} are the valence band and conduction band potentials, respectively; X is the absolute electronegativity of the semiconductor (6.59 eV for WO_3); E^e is the energy of free electrons on the hydrogen scale (approximately 4.5 eV vs. NHE); E_g is the optical band gap obtained from the Tauc plot.

The calculation results indicate that Fe-WO_3 has a VB potential of 3.47 V vs. NHE and a CB potential of 0.38 V vs. NHE, while $BiVO_4$ has a VB potential of 2.69 V vs. NHE and a CB potential of 0.39 V vs. NHE. The staggered band alignment forms a typical Type-II heterojunction, which provides an energetic basis for the directional separation and

migration of photogenerated carriers. Under visible light irradiation, both semiconductors are excited to generate electron–hole pairs. Driven by the built-in electric field, photogenerated electrons on the CB of $BiVO_4$ spontaneously transfer to the CB of Fe-WO_3, and holes on the VB of Fe-WO_3 migrate to the VB of $BiVO_4$, realizing effective spatial separation of electrons and holes and greatly suppressing bulk carrier recombination.

Combined with the radical scavenging results, the $\cdot O_2^-$-dominated photo-Fenton degradation mechanism is proposed. The reaction pathways and synergistic effects are as follows:

3.5.1Superoxide radical generation as the dominant path

Surface Fe^{3+} reacts with H_2O_2 to generate hydroperoxyl radical ($HO_2\cdot$) and Fe^{2+}. The generated $HO_2\cdot$ dissociates into $\cdot O_2^-$ under alkaline conditions, and the alkaline environment improves the stability of $\cdot O_2^-$, which effectively compensates for the performance loss caused by ·OH quenching. This is the core reason why the system maintains high degradation efficiency under alkaline conditions. The generated $\cdot O_2^-$ is the main active species for attacking and degrading TC molecules.

3.5.2Auxiliary oxidation of hydroxyl radicals and holes

The Fe^{2+} generated in the above reaction undergoes the classic

Fenton reaction with H_2O_2 to produce ·OH. Meanwhile, the holes accumulated on the VB of $BiVO_4$ can directly oxidize adsorbed TC molecules. Both ·OH and h^+ play a synergistic role in the degradation process, but their contribution is weaker than that of $\cdot O_2^-$.

3.5.3Heterojunction promotes iron cycle efficiency

The photogenerated electrons enriched on the CB of Fe-WO_3 can rapidly reduce Fe^{3+} to Fe^{2+}, which greatly accelerates the Fe^{3+}/Fe^{2+} redox cycle, breaks the rate-limiting step of traditional Fenton reactions, and ensures the continuous generation of active species.

Finally, under the synergistic oxidation of $\cdot O_2^-$, ·OH and h^+, TC molecules are gradually degraded and finally mineralized into CO_2, H_2O and other small molecular products.

$$WO_3 + h\nu \rightarrow WO_3\left(e_{CB}^-\right) + WO_3\left(h_{VB}^+\right) \quad (1)$$

$$BiVO_4 + h\nu \rightarrow BiVO_4\left(e_{CB}^-\right) + BiVO_4\left(h_{VB}^+\right) \quad (2)$$

$$Fe^{3+} + H_2O_2 \rightarrow Fe^{2+} + HO_2\cdot + H^+ \quad (3)$$

$$HO_2\cdot \rightarrow \cdot O_2^- + H^+ \quad (4)$$

$$Fe^{3+} + H_2O_2 \rightarrow Fe^{3+} + \cdot OH + OH^- \quad (5)$$

$$\cdot OH / h^+ / \cdot O_2^- + TC \rightarrow CO_2 + H_2O + \text{molecular products} \quad (6)$$

4.Conclusions

In summary, Fe-doped $WO_3/BiVO_4$ heterojunction photo-Fenton catalysts were successfully fabricated via a facile hydrothermal method

in this work. When the mass ratio of $BiVO_4$ to Fe-WO_3 was 0.5, the 0.5 BFW composite exhibited the optimal photo-Fenton activity: the degradation efficiency of 50 mg/L tetracycline (TC) reached 94.5% within 60 min under simulated visible light irradiation. Its apparent reaction rate constant was 7.0 times that of pristine WO_3 and 1.35 times that of single Fe-doped WO_3. Meanwhile, the composite catalyst possessed wide pH adaptability and maintained high degradation activity after five consecutive cycles, showing excellent structural stability and reusability.

The enhanced photo-Fenton performance can be attributed to the following synergistic effects. First, Fe ion doping narrows the band gap of WO_3, extends the visible light response range, and provides abundant iron active sites for the Fenton reaction. Second, the Type-II heterojunction formed between Fe-WO_3 and $BiVO_4$ effectively promotes the spatial separation and transfer of photogenerated electron-hole pairs, significantly suppresses carrier recombination, and continuously provides electrons for the Fe^{3+}/Fe^{2+} redox cycle to break the rate-limiting step of the traditional Fenton reaction. Third, the lattice distortion and enriched oxygen vacancies at the heterointerfaces supply more reactive active sites for the degradation process.

Radical scavenging experiments confirm that superoxide radicals ($\cdot O_2^-$)

play a dominant role in the TC degradation process, while hydroxyl radicals (·OH) and holes (h^+) also make synergistic contributions. This study demonstrates that the dual modification of ion doping and heterojunction construction is an effective strategy to improve the photo-Fenton performance of WO_3-based catalysts, and the composite system has promising application prospects in the field of alkaline antibiotic wastewater treatment.

Credit authorship contribution statement

Junlin Zhu: Conceptualization, Methodology, Data curation, Writing-review & editing, Resources. **Zhiqiang Wei:** Investigation, Date curation, Writing-Original draft preparation. **Meilin Yan:** Validation. **Youcai Zhang:** Validation. **Jinglong Bai:** Date curation. **Wangjun Feng:** Writing-review & editing, Resources. **Huining Zhang:** Writing-review & editing, Resources

Declaration of Interest Statement

The authors declare that they have no known competing financial interests or personal relationships that could have appeared to influence the work reported in this paper.

Acknowledgements

This work was supported by National Natural Science Foundation of China (52268042, 52468035), the Hongliu Outstanding Young Talents Funding of Lanzhou University of Technology, Gansu Provincial University Teachers' Innovation Fund, and Young Faculty Interdisciplinary Research Cultivation Program of Lanzhou University of Technology (XKJC-25032).

References:

[1] Browne J, et al. Global antibiotic consumption 2000 to 2015: an analys is of national pharmaceutical sales data[J]. *Lancet Infectious Diseases*, 2 018, 18(10): 1075-1084. DOI: 10.1016/S1473-3099(18)30413-0

[2] Liu Y, et al. Global trends in antibiotic consumption during 2016–2023 and future projections through 2030[J]. Proceedings of the National Aca demy of Sciences of the United States of America (PNAS), 2024, 121 (16): e2312704121. DOI: 10.1073/pnas.2312704121

[3] Ding M , Wei Z , Liu D ,et al.Electronic modulation towards MOFs a s template derived CoP via engineered heteroatom defect for a highly e fficient overall water splitting[J].Journal of Energy Chemistry, 2025, 101 (000):598-607.DOI:10.1016/j.jechem.2024.10.010.

[4] Daghrir R, Drogui P. Tetracycline antibiotics in the environment: a revi ew[J]. Environmental Chemistry Letters, 2013, 11(3): 209-227. DOI: 10. 1007/s10311-013-0409-4

[5] 陈永强，等。四环素类抗生素的环境行为、生态毒性及去除技术研究进展 [J]. 环境工程学报，2021，15 (7): 2245-2260. DOI: 10.12030/j.cjee.2 02101087

[6] Guo X, et al. Ecotoxicological effects of tetracycline on aquatic organis ms: A review[J]. Environmental Pollution, 2022, 306: 119405. DOI: 10. 1016/j.envpol.2022.119405

[7] Martinez J L. Environmental pollution by antibiotics and by antibiotic r esistance determinants[J]. Environmental Pollution, 2009, 157(11): 2893-2902. DOI: 10.1016/j.envpol.2009.05.051

[8] 杨凯，等。水环境中四环素类抗生素耐药基因的污染特征与传播机制研究进展 [J]. 环境化学，2023, 42 (5): 1627-1639. DOI: 10.7524/j.issn.0254-6108.2022091302

[9] 王兵，等。传统污水处理工艺对抗生素及耐药基因去除效果的研究进展 [J]. 环境科学与技术，2020, 43 (S1): 132-140.

[10] Oturan M A, Aaron J J. Advanced oxidation processes in water/wastewater treatment: Principles and applications. A review[J]. Critical Reviews in Environmental Science and Technology, 2014, 44(23): 2577-2641. DOI: 10.1080/10643389.2013.829765

[11] Neyens E, Baeyens J. A review of classic Fenton's peroxidation as an advanced oxidation technique[J]. Journal of Hazardous Materials, 2003, 98(1-3): 33-50. DOI: 10.1016/S0304-3894(02)00282-0

[12] 李来胜，等。非均相光芬顿催化降解水中四环素类抗生素的研究进展 [J]. 催化学报，2023, 44 (2): 267-282. DOI: 10.1016/S1872-2067 (22) 64170-9

[13] Rizvi H I, Munir R M, Iqbal T, et al. Novel existence of Mn and Cu in WO_3 nanostructures for promising photocatalytic activity against MB dye and Levofloxacin antibiotic[J]. Journal of Alloys and Compounds, 2024, 993: 174549.

[14] Xie R, Fang K, Liu Y, et al. Z-scheme In_2O_3/ WO_3 heterogeneous photocatalysts with enhanced visible-light-driven photocatalytic activity toward degradation of organic dyes[J]. Journal of Materials Science, 2020, 55(26): 11919-11937.

[15] Zhang Y, Wei Z, Yan M, et al. One-Step Hydrothermal Synthesis of A $g_4V_2O_7$/$BiVO_4$ Type-II Heterojunctions with Boosted Visible-Light Photo catalytic Activity[J]. The Journal of Physical Chemistry C, 2026, 130(3 5): 12387-12399.

[16] Gu H, Lin Z, Li Y, et al. Research progress of NiS cocatalysts in pho tocatalysis[J]. Physica status solidi (a), 2024, 221(10): 2400187.

[17] Fatima M, Aziz M H, Zahir F, et al. Synergistic $BaFe_2O_4$/$BiVO_4$ Heter ojunctions for Accelerated Visible-Light Tetracycline Degradation and M ultifunctional Bioactivity[J]. Physica B: Condensed Matter, 2026: 41939 7.

[18] Zhou T, Zhao Z, Deng X, et al. Synergistic effect of type-II heterojunc tion and cocatalyst loading on $BiVO_4$-based photoanode for enhanced p hotoelectrochemical water splitting H_2 evolution[J]. International Journal of Hydrogen Energy, 2026, 199: 152901.

[19] Zeng L, Wang C, Hu J. Ultrasonic degradation of tetracycline combinin g peroxymonosulfate and $BiVO_4$ microspheres[J]. Journal of Water Proc ess Engineering, 2023, 56: 104428.

[20] Yao M , Li Q , Hou G ,et al.Dopant-Controlled Morphology Evolution of WO_3 Polyhedra Synthesized by RF Thermal Plasma and Their Sensi ng Properties[J].ACS Applied Materials & Interfaces, 2015.DOI:10.1021/ am5081277.

[21] NGUYEN L T, NGUYEN N T, TRAN T N N, et al. An In-Depth Stu dy of the Crystal Structure, Oxidation States, Defects, and Photocatalyti c Activity of Fe-Doped WO_3 Nanomaterials[J]. ACS Applied Nano Mat erials, 2026, 9(16): 7304-7317. DOI:10.1021/acsanm.6c00596.

[22] Fan X , Chen Q , Zhu F ,et al.Preparation of Surface Dispersed WO_3 /$BiVO_4$ Heterojunction Arrays and Their Photoelectrochemical Performan ce for Water Splitting[J].Molecules, 2024, 29(2).DOI:10.3390/molecules2 9020372.

[23] Sun Y , Murphy C J , Reyes-Gil K R ,et al.Photoelectrochemical and structural characterization of carbon-doped WO3 films prepared via spra y pyrolysis - ScienceDirect[J].International Journal of Hydrogen Energy, 2009, 34(20):8476-8484.DOI:10.1016/j.ijhydene.2009.08.015.

[24] Masato,Takeuchi,and,et al.Preparation of the visible light responsive N_3− -doped WO_3 photocatalyst by a thermal decomposition of ammonium p aratungstate[J].Applied Catalysis B Environmental, 2011.DOI:10.1016/j.ap catb.2011.08.004.

[25] Xuan X , Yaofang S , Zihong F ,et al.Mechanisms for O_2 and OH pro duction on flowerlike $BiVO_4$ photocatalysis based on Electron Spin Res onance[J].Frontiers in Chemistry, 2018, 6:64.DOI:10.3389/fchem.2018.00 064.

[26] 龙子洋 李全政 张成亮 史海峰.BiVO4/WO3-x. S型异质结通过增强内建电场提升光热催化活性[J]. 2025.

[27] Ye K H , Li H , Huang D ,et al.Enhancing photoelectrochemical water splitting by combining work function tuning and heterojunction engine ering[J].Nature Communications, 2019, 10(1).DOI:10.1038/s41467-019-11 586-y.

[28] Jayachitra R , Suriya M , Prasannan A ,et al.Membranes with Nanopart icles of Tungsten Oxide–Iron Oxide for CO2 Selective Permeation and Degradation of Azo Phenols[J].[2026-10-13].

[29] Wang J C , Shi W , Sun X Q ,et al.Enhanced Photo-Assisted Acetone Gas Sensor and Efficient Photocatalytic Degradation Using Fe-Doped H exagonal and Monoclinic WO3 PhaseJunction[J].Nanomaterials, 2020, 10 (2):398.DOI:10.3390/nano10020398.

[30] Zhao X , Wei Z , Qiao H ,et al.Study on the Morphological Control a nd Photocatalytic Mechanism of BiOI Nanomaterials Synthesized by the Co-precipitation Method[J].Ionics, 2026, 32(6):5975-5987.DOI:10.1007/s 11581-026-07129-3.

[31] Shahine I , Jradi S , Beydoun N ,et al.Plasmon-Enhanced Photolumines cence and Photocatalysis Reactions in Metal-Semiconductor Nanomateria ls: UV-Generated Hot Electron in Gold-Zinc Oxide[J].ChemPhotoChem, 2020, 4(3).DOI:10.1002/cptc.201900252.

[32] Barham J P , Knig B .Synthetic Photoelectrochemistry[J].Angewandte C hemie International Edition, 2020, 59(29).DOI:10.1002/anie.201913767.

[33] Zhang, Runpei,Wu, Shujuan,Wei, Zhiqiang,等.Sunlight-powered RhB deg radation by a novel BiOI@$ZnFe_2O_4$ Z-scheme heterojunction[J].Journal of Materials Science.Materials in Electronics, 2026(10):37.DOI:10.1007/s 10854-026-17119-w

[34] Zhao X, Wei Z, Qiao H, et al. Loading-Dependent Interfacial Regulatio n and Visible-Light Photocatalytic Behavior of BiOI@ g-C_3N_4 Composit e Photocatalysts[J]. Materials Research Bulletin, 2026: 114426.

[35] Yu Q , Zhao Z , Wei Z ,et al.Enhanced photo-Fenton degradation of t etracycline using MIL-101(Fe)/g-C_3N_4/FeOCl double Z-scheme heterojun ction catalyst[J].Applied Surface Science,2025,688(000).DOI:10.1016/j.aps usc.2025.162386.

[36] Ni Q , Ke X , Qian W ,et al.Insight into tetracycline photocatalytic de gradation mechanism in a wide pH range on BiOI/BiOBr: Coupling DF T/QSAR simulations with experiments[J].Applied Catalysis, B: Environm ental, 2024, 340(000):16.DOI:10.1016/j.apcatb.2023.123226.

[37] Dai K, Lu L, Liang C, et al. A high efficient graphitic-C_3N_4/BiOI/grap hene oxide ternary nanocomposite heterostructured photocatalyst with gr aphene oxide as electron transport buffer material[J]. Dalton Transaction s, 2015, 44(17): 7903-7910.

[38] Aslam I, Cao C, Tanveer M, et al. A novel Z-scheme WO_3/$CdWO_4$ ph otocatalyst with enhanced visible-light photocatalytic activity for the deg radation of organic pollutants[J]. RSC advances, 2015, 5(8): 6019-6026.